International Journal of Remote Sensing
Vol. 33, No. 1, 10 January 2012, 81–100

Taylor & Francis
Taylor & Francis Group

A framework for automated assessment of post-earthquake building damage using geospatial data

PINLIANG DONG*†‡ and HUADONG GUO†
†Center for Earth Observation and Digital Earth (CEODE), Chinese Academy of Sciences, Beijing 100190, PR China
‡Department of Geography, University of North Texas, Denton, TX 76203, USA

(*Received 4 August 2010; in final form 4 February 2011*)

Based on the triangulated irregular network (TIN) model, barycentric coordinates and random points, a new method was developed for more accurate characterization of 3D shape signatures of buildings using Light Detection and Ranging (LiDAR) data and Geographic Information System (GIS). The new method was applied to four simulated building models with flat, pent, gable and hip roofs to test the detection of changes in 3D building shapes in a post-earthquake scenario: (1) a three-storey building model becomes two-storey after losing the first floor; (2) a severe damage of a two-storey building model; and (3) a total collapse of a two-storey building model. The new method was then applied to real LiDAR data from four buildings in Harris County, TX, USA. All the changes in 3D shapes of the models and real buildings were successfully detected using 3D shape signatures. Sensitivity analyses were carried out to test the influence of LiDAR point density and new points in TIN triangles on 3D shape signatures. The results suggest that LiDAR point density of 0.5 point m^{-2} or higher can generate stable 3D shape signatures of buildings, and that the density of the new points in TIN triangles does not affect 3D shape signatures significantly. Built upon the new method and results, a framework was proposed for an automated assessment of post-earthquake building damage using geospatial data. A flowchart was presented to provide more details of the framework, and the advantages and limitations of the framework were also discussed. It is expected that the framework can be effectively applied to post-earthquake building damage assessment and other disaster scenarios that involve major changes in 3D building shapes.

1. Introduction

Earthquakes can cause destruction and take human lives by structurally damaging buildings and dwellings, and causing other disasters such as fires and tsunamis. Since 1980, there have been eight strong earthquakes with deaths over 10 000: Mexico (1985), Armenia (1988), Iran (1990), Turkey (1999), Indian Ocean (2004, earthquake and tsunami), South Asia (2005), China (2008) and Haiti (2010). After a catastrophe like a strong earthquake, one of the top priorities is to start search and rescue operations for people trapped in wrecked buildings. Space- and airborne sensors have been used to identify and assess natural disasters like earthquakes in the last decades. Although

*Corresponding author. Email: pdong@unt.edu

International Journal of Remote Sensing
ISSN 0143-1161 print/ISSN 1366-5901 online
http://www.tandf.co.uk/journals
http://dx.doi.org/10.1080/01431161.2011.582188

real-time support for ground search and rescue is still a difficult task for current remote sensing systems, it is hoped that data from space- and airborne platforms can provide important information for rescue and recovery efforts. Therefore, timely assessment of building damage is essential for earthquake recovery programmes.

A few studies have been conducted on post-earthquake building damage assessment using remotely sensed images (Aoki *et al*. 1998, Huyck *et al*. 2002, Matsuoka and Yamazaki 2002, Yusuf *et al*. 2002, Adams 2004, Saito *et al.* 2004, Adams *et al*. 2005, 2006, Kaya *et al*. 2005). Kaya *et al*. (2005) compared building collapse estimates derived from pre-earthquake and post-earthquake SPOT (Satellite Pour l'Observation de la Terre) HRVIR (high resolution visible and infrared) data from the 1999 Izmit, Turkey earthquake with government statistics, and found that the results for the proportion of collapsed buildings were similar. However, building damage estimation at the individual building level is difficult because the spatial resolution of SPOT images was not high enough for detecting damages to many buildings. Since 2002, high-resolution images such as QuickBird and IKONOS images have been used for earthquake damage assessment (Chiroiu *et al*. 2002, Adams *et al*. 2004). It seems that the time-consuming visual interpretation methods are still the major methods for building damage assessment, partly because traditional image classification methods cannot be directly applied to high-resolution images. Turker and Sumer (2008) developed a building-based earthquake damage assessment system in MATLAB (Mathworks, Natick, MA, USA) using watershed segmentation of the post-event aerial images and GIS and tested the system with data from Golcuk, an area hit by the 1999 Izmit, Turkey earthquake. The system successfully provided a detection rate of 63.3% for damaged buildings, and 87.3% for undamaged buildings. However, since the watershed segmentation method is based on building shadows which can be very complex, they also reported several limitations of this method. Indeed, building shadows can be difficult to detect if the buildings are close to one another, and if the illumination conditions are poor.

The all-weather capability of radar systems, along with other features, provides an important option for building damage assessment in bad weather. Guo *et al*. (2009) conducted research on detecting collapsed urban buildings using air- and spaceborne synthetic aperture radar (SAR) data after the 2008 Wenchuan earthquake (magnitude scale (M_s) 8.0) in China. Since pre-earthquake SAR data were not available in the area, they focused on detecting collapsed buildings using post-earthquake SAR data alone. Their results show that longer wavelength SAR data (such as L-band) have better performance than shorter wavelengths in detecting collapsed buildings, but results from multi-polarization spaceborne SAR data are more complex due to variations in building type, material and structure. Wang *et al*. (2009) used high-resolution (0.5 m) airborne X-band SAR images for the interpretation of building damage after the 2008 Wenchuan earthquake, China. They concluded that, without Interferometric Synthetic Aperture Radar (InSAR) data, it is very difficult to detect damaged buildings even with high-resolution SAR images. Dong *et al*. (2011) used 10 m resolution Advanced Land Observing Satellite (ALOS) Phased Array type L-band Synthetic Aperture Radar (PALSAR) images and 1 m resolution TerraSAR-X images to extract earthquake damage information after the M_s 8.0 Wenchuan earthquake, China. Based on change detection using pre- and post-earthquake SAR images, they found that high spatial resolution images such as 1 m resolution TerraSAR-X images can provide useful information on areas of building damage. It should be noted, however, that radar

layover effects and shadows can hamper the interpretation of SAR images, particularly in mountain environments.

Visual interpretation of optical and SAR images is helpful in building damage assessment, but the process is labour-intensive because automated identification of damaged buildings is difficult using optical or SAR images alone. Sometimes, visual interpretation of optical images may not detect major changes in the 3D shapes of buildings. For example, after the 2008 Wenchuan earthquake of magnitude 8.0 in China, many buildings in the downtown area of Beichuan County lost the first floors but still appeared intact on SAR images (Wang *et al*. 2009). In such cases, it would be very difficult to make accurate assessment of building damage using optical or radar images. Photogrammetric methods may be useful, but data collection and processing can be time-consuming. InSAR could be an alternative data source because of its ability to provide elevation data, but the data quality and the elevation accuracy derived from InSAR are not as high as those of Light Detection and Ranging (LiDAR) data (Stilla and Jurkiewicz 1999, Stilla *et al*. 2003).

LiDAR point clouds are usually pre-processed to create a digital elevation model (DEM) and a digital surface model (DSM). The difference between DSM and DEM is called normalized digital surface model (nDSM), which represents the height of ground objects such as buildings and trees. Figure 1 is an example of nDSM in Port-au-Prince, Haiti, obtained from the LiDAR data collected after the 2010 Haiti earthquake with a density of 2 points m^{-2}. The red circles in figure 1 represent

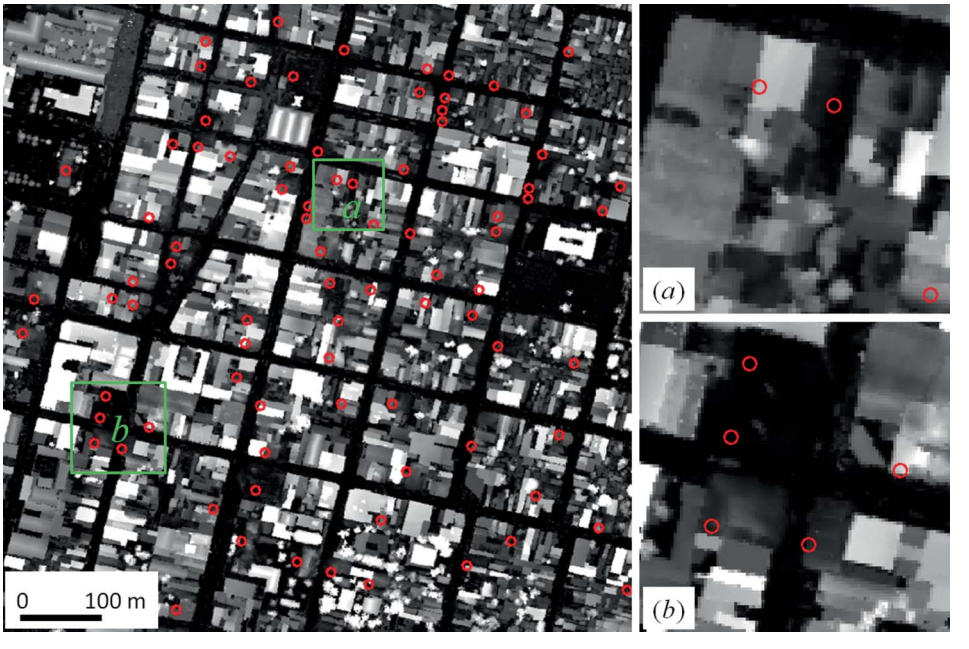

Figure 1. A normalized digital surface model (nDSM) in Port-au-Prince derived from Light Detection and Ranging (LiDAR) data collected after the 2010 Haiti earthquake. Red circles show damaged buildings interpreted from air photos.
Source: Original data were obtained with permission from the Chester Carlson Center for Imaging Sciences at the Rochester Institute of Technology (RIT).

the locations of severely damaged buildings interpreted from aerial photographs. While the nDSM clearly shows the height distribution of the buildings, the example indicates that it is difficult to interpret damaged buildings from post-earthquake LiDAR data alone without pre-earthquake LiDAR data or 3D building information from GIS databases.

Extracting buildings from remotely sensed data has become a significant research field in the last two decades. Many algorithms for building extraction have been proposed, including mathematical morphology (Weidner and Förstner 1995, Pesaresi and Benediktsson 2001), DSM segmentation (Baltsavias *et al*. 1995, Sithole and Vosselman 2004, Tovari and Pfeifer 2005), active contours or snakes (Nixon and Aguado 2002, Oriot 2003, Ahmadi *et al*. 2010, Kabolizade *et al*. 2010), Dempster–Shafer method (Rottensteiner *et al*. 2005), neural networks (Barsi 2004, Bellman and Shortis 2004), knowledge-based systems (Baltsavias 2004, Mayer 2008) and multi-scale method (Vu *et al*. 2009). A review of most of the methods can be found in Ioannidis *et al*. (2009). With the increasing demand of 3D city models and availability of LiDAR data, 3D building reconstruction has received extensive attention, and many method for building reconstruction have been proposed (Gruen 1998, Haala and Brenner 1999, Maas and Vosselman 1999, Stilla and Jurkiewicz 1999, Stilla *et al*. 2003, Suveg and Vosselman 2004, Brenner 2005, Madhavan *et al*. 2006, Sugihara and Hayashi 2008, Alexander *et al*. 2009, Jang and Jung 2009, Pu and Vosselman 2009, Tang *et al*. 2010). Meanwhile, building damage assessment based on building reconstruction and image classification has become a research topic. Li *et al*. (2008) proposed a method for building damage assessment based on building reconstruction using IKONOS images and LiDAR data. However, their method assumed that both pre-earthquake and post-earthquake LiDAR data are available, which might be difficult in many cases. Chen and Hutchinson (2010) proposed a probabilistic classification method for image-based urban structural damage identification using bi-temporal satellite images. They also identified future research needs regarding building-level assessment through an automated workflow.

In addition to the progress in building extraction from remotely sensed data, developments in web technology have shown some new trends in geospatial data infrastructure in recent years. While spatial data infrastructure (SDI) has been mainly a top-down, government-driven initiative, a bottom-up path involving geospatial professionals and expert amateurs has emerged (Gould 2006). Introductions and more in-depth analyses of volunteered geographic information (VGI) (Goodchild 2007, Elwood 2008, Flanagin and Metzger 2008) and NeoGeography (Turner 2006, Goodchild 2009) are beginning to appear. Grassroots citizens can now make contributions to the global geospatial data infrastructure. For example, Internet users can create 3D models of individual buildings for many cities in the world using Google Building Maker, save the 3D models in the Google warehouse and share the models with other users.

Given that information on pre-earthquake 3D shapes of buildings is available from geospatial databases as building parameters or 3D building models, and that pre-earthquake LiDAR data may not be available, the challenge is to detect major damages to buildings using existing geospatial data and post-earthquake LiDAR data in an automated process. The objectives of this research are (1) to develop an effective and efficient approach to detecting changes of 3D building shapes using simulated building models and real LiDAR data; and (2) to propose a framework for automated assessment of post-earthquake building damage using geospatial data.

2. Automated detection of changes in 3D building shapes

2.1 *3D shape signatures*

Osada *et al*. (2002) described a method for computing 3D shape signatures and dissimilarity measures for arbitrary objects in computer graphics. The basic idea behind 3D shape signatures is to transform an arbitrary 3D object into a parameterized function that can easily be compared with other objects. A 3D shape signature is represented as a probability distribution sampled from a shape function measuring geometric properties of the 3D object. In the work of Osada *et al*. (2002), five shape functions were proposed. Dong (2009, 2010) used one function, D2, to measure the distance between two random points selected from LiDAR point clouds of individual tree crowns. After a certain number of iterations (e.g. 10 000) for D2 calculation, the sorted distances between the point pairs are put into 50 histogram bins to show the frequency distribution, which can be further converted into a probability distribution. The probability distribution is then used as the 3D shape signatures of the object. It has been shown that 3D shape signatures can effectively describe 3D shapes of tree crowns (Dong 2009, 2010). In §2.2, 3D shape signatures of simulated building models will be calculated to support automated detection of changes in 3D building shapes.

2.2 *3D shape signatures of simulated building models*

Four common 3D building models with flat, pent, gable and hips roofs were generated as raster surfaces similar to nDSMs derived from LiDAR data and were referred to as 'two-storey models' (see the middle column in figure 2). The footprint size of the models is 14 × 24 m, and the heights of the two-storey models are different: flat roof – 5 m; pent roof: 5–10 m; gable roof: 5–12 m; and hip roof: 5–12 m. In addition, three sets of models were also generated to test the detection of changes in 3D shapes in different building damage scenarios: (1) three-storey models (see the first column in figure 2) – these models were 3 m higher than the two-storey models and were used to study changes in 3D building shapes when a three-storey building loses the first floor and becomes a two-storey building; (2) damaged models (see the third column in figure 2) – severe damage of two-storey models; and (3) collapsed models – total collapse of two-storey models into debris with random variation of thickness between 1 and 2 m (not shown in figure 2).

A LiDAR point density of 2 points m^{-2} is used to generate random points on building roofs and footprint boundary for 3D shape signature analysis. Each model was run 3 times for 3D shape signature calculation. In previous research (Dong 2009, 2010), it has been shown that 10 000 point pairs should be enough for generating stable 3D shape signatures for tree crowns. Because real buildings may have different sizes and shapes, 100 000 random point pairs were used for distance calculation in each model run. Comparisons of 3D shape signatures for the building models are shown in figure 3. As can be seen in figure 3, the 3D shape signatures generated from 100 000 random point pairs are very stable (the three curves from three model runs are almost identical). From the correlation coefficients (r) of the 3D shape signatures, it can be seen that the differences between the three-storey models and the two-storey models, and between the two-storey models and collapsed models are relatively easy to tell. However, there are only subtle differences ($r > 0.99$) between two-storey models and damaged models.

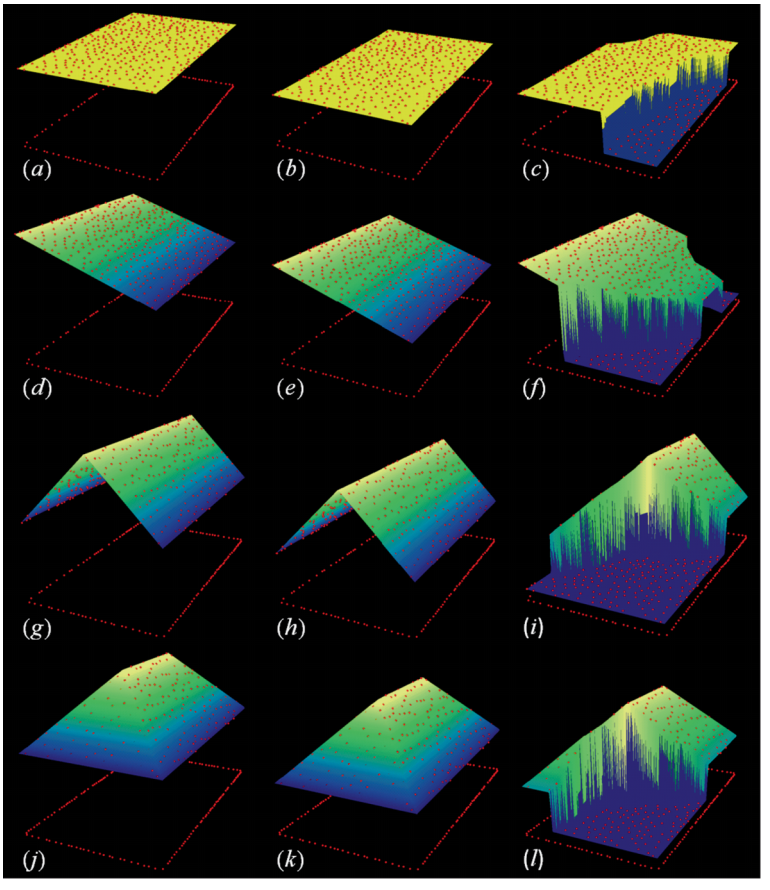

Figure 2. Simulated 3D building models with flat (first row), pent (second row), gable (third row) and hips roofs (fourth row). First column: three-storey models; second column: two-storey models; third column: damaged models. Models for total collapse are not shown here.

An explanation on the similarity between the 3D shape signatures of two-storey models and damaged models is that damaged two-storey buildings only involve partial change in heights compared with the original two-storey buildings, whereas the change from three-storey models to two-storey models and from two-storey models to collapsed models involves significant changes in building heights, resulting in reduced frequencies of relatively long distances between random point pairs. This can also be seen from the 3D shape signatures (probability functions) in the first and third columns of figure 3. In addition, the lack of sampling points on walls and other vertical faces may also affect the frequency distribution of distances between point pairs when a certain number of iterations (such as 100 000) are used to collect the random point pairs. Therefore, it is anticipated that differences between the original two-storey building models and the damaged building models can be better revealed if the points on vertical faces are also used for 3D shape signature analysis. Based on this idea, a new approach is proposed in §2.3.

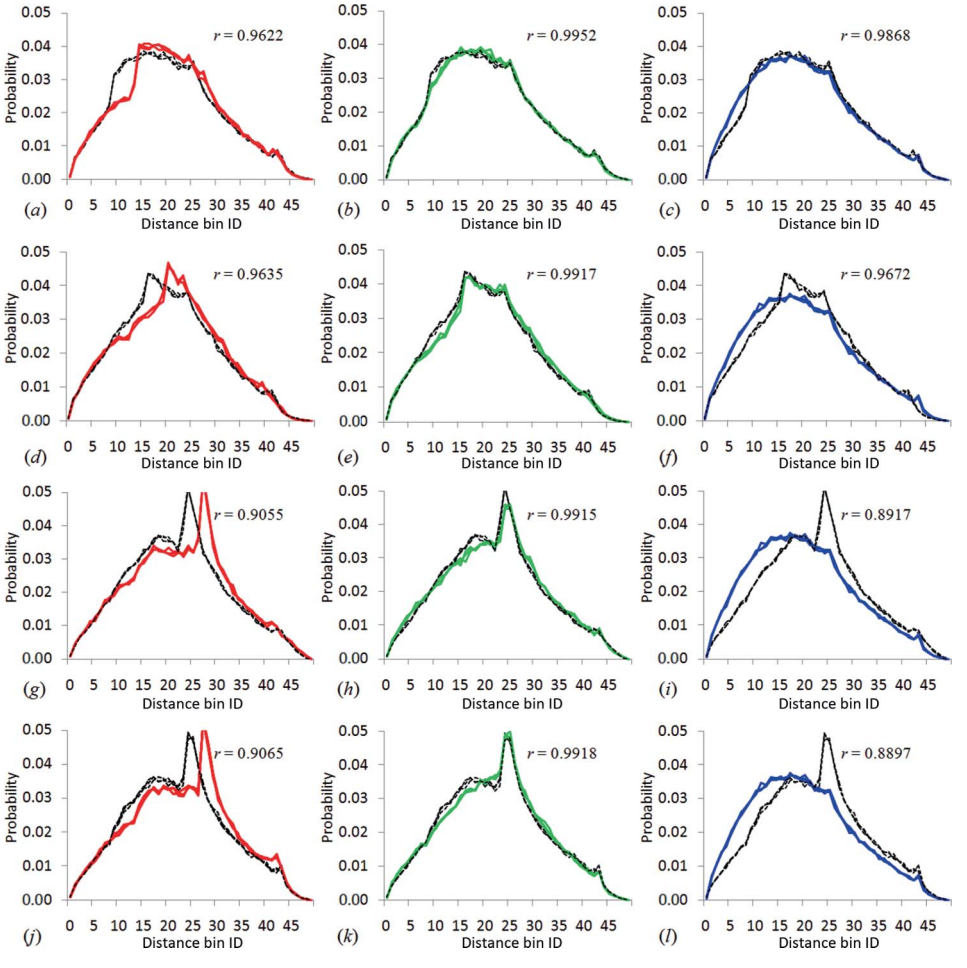

Figure 3. Comparisons of 3D shape signatures obtained from the building models in figure 2. First row: flat roofs; second row: pent roofs; third row: gable roofs; and fourth row: hip roofs. First column: three-storey models (red) vs. two-storey models (black); second column: two-storey models (black) vs. damaged models (green); third column: two-storey models (black) vs. collapsed models (blue). r is the correlation coefficient between the 3D shape signature curves of two models.

2.3 *A new approach based on TIN models and barycentric coordinate system*

In GIS, 3D data are usually presented using contours, raster surfaces or triangulated irregular networks (TINs). To obtain random sampling points from vertical or near vertical faces of the buildings models in figure 2, the TIN data model is the only option because (1) contours cannot present vertical faces, and (2) rasters can show vertical faces as edges where cell values jump from low to high, but data on the vertical or nearly vertical faces cannot be represented by rasters.

In the TIN model, triangles are created from a set of points through Delaunay triangulation. Given a 2D or 3D triangle with vertices p_1, p_2 and p_3, any point p in the triangle can then be specified by a weighted sum of these three vertices, that is,

$$p = t_1 p_1 + t_2 p_2 + t_3 p_3, \tag{1}$$

where $t_1 + t_2 + t_3 = 1$. t_1, t_2 and t_3 are called barycentric coordinates (Bradley 2007), and each of which indicates how much relative influence the corresponding triangle vertex contributes to the location of the point p. If the 3D Cartesian coordinates of p_1, p_2, p_3 and p are (x_1, y_1, z_1), (x_2, y_2, z_2), (x_3, y_3, z_3) and (x, y, z), respectively, x, y, z can be calculated using the following equations:

$$x = t_1 x_1 + t_2 x_2 + (1 - t_1 - t_2) x_3, \tag{2}$$

$$y = t_1 y_1 + t_2 y_2 + (1 - t_1 - t_2) y_3, \tag{3}$$

$$z = t_1 z_1 + t_2 z_2 + (1 - t_1 - t_2) z_3. \tag{4}$$

Once the three vertices are obtained for each triangle in a TIN model, random points can be generated in the triangle using equations (2)–(4). In other words, random points can be created anywhere on the TIN surface, including vertical walls of the original building models and vertical faces of damaged buildings. This allows more representative sampling of the 3D shape because every part (except the bottom plane) of the building is covered with data points. In computer implementation, t_1 and t_2 are random numbers between 0 and 1. If $t_1 + t_2 > 1$, then t_1 is replaced with $1 - t_1$, and t_2 replaced with$1 - t_2$. This ensures that barycentric coordinates will be uniformly distributed in the triangle (instead of creating clusters). Figure 4 is a flowchart showing the process from data input to 3D shape signature analysis for each building. Random points on the rooftop (P_M) and along the footprint boundary (P_N) are used to generate TIN models. Based on the point density calculated from the rooftop points, new points (P_T) are generated in each TIN triangle. Finally, P_M, P_N and P_T are combined for 3D shape signature analysis. Figure 5 shows selected TIN models and random data points for two-storey flat and gable building models and

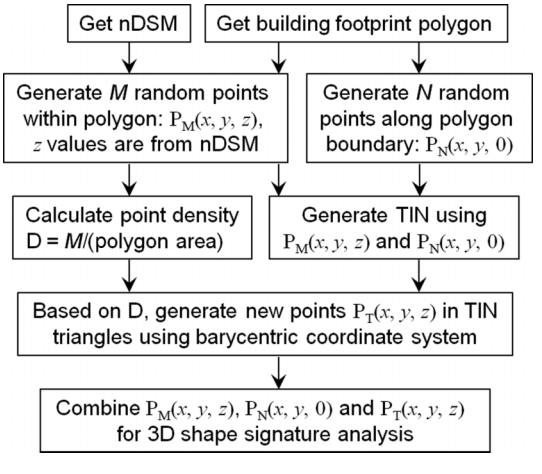

Figure 4. Flowchart of 3D shape signature analysis for each building.
Note: TIN, triangulated irregular network; nDSM, normalized digital surface model.

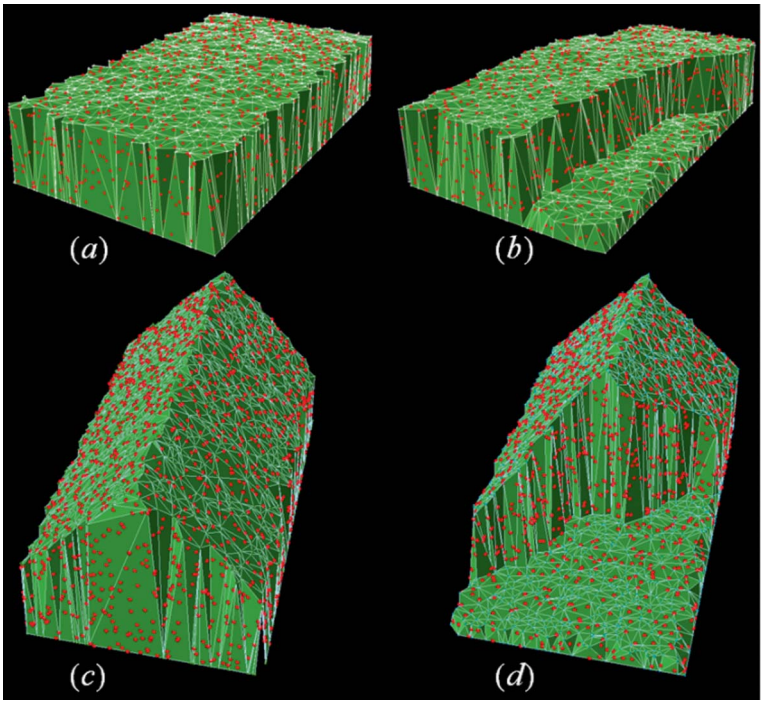

Figure 5. New random points generated using the triangulated irregular network (TIN) model and barycentric coordinates. (*a*) Original flat roof model, (*b*) damaged flat roof model, (*c*) original gable roof model and (*d*) damaged gable roof model.

their damaged versions. As can be seen in figure 5, new random points were generated on vertical and near-vertical faces of the building, as if the building models are covered with a digital 'blanket' and random points are available on the surface of the blanket.

Using this new approach, new 3D shape signatures of the building models were calculated (figure 6). Point density D is set to 2 points m^{-2} in each model. Like the old approach in §2.2, each model was run 3 times for 3D shape signature calculation, and 100 000 random point pairs were used for distance calculation in each model run. Compared with figure 3, it can be seen that the building models were well separated in all tested damage situations: (1) a three-storey building becomes two-storey due to the loss of the first floor; (2) severe damage of a two-storey building; and (3) total collapse of a two-storey building.

This new method was implemented using Microsoft Visual Basic for Applications (VBA) with ESRI's ArcObjects 9.3 in the ArcGIS 9.3 software. In terms of processing time, it takes about 0.9 s to process 2000 points on a desktop computer with 2.53 GHz processor and 4 GB RAM, including generation of random points (<0.1 s), creation of TIN (about 0.2 s), calculation of barycentric coordinates (about 0.2 s) and calculation of 3D shape signatures using 100 000 random point pairs (about 0.4 s). In other words, the 3D shape signatures of each building in figure 5 can be obtained in less than 1 s, which is very promising for real-world applications such as post-earthquake building damage assessment.

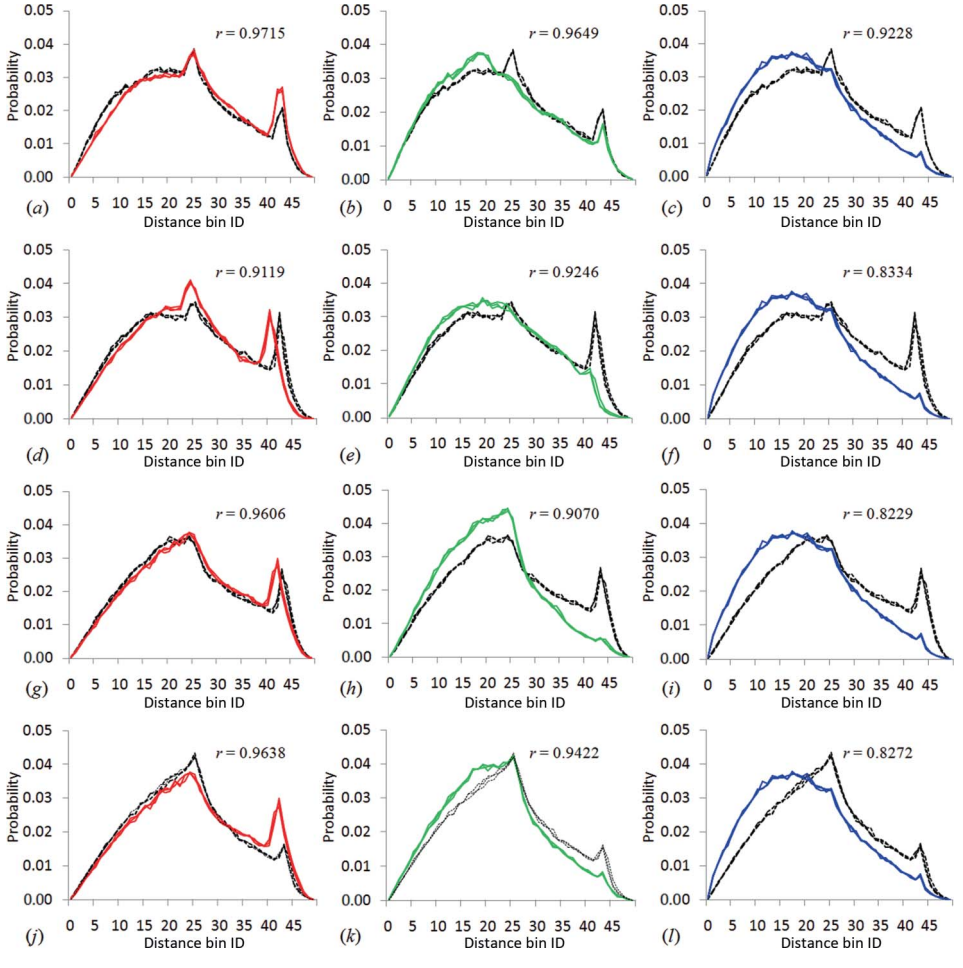

Figure 6. Comparisons of 3D shape signatures obtained from the building models in figure 2 using the triangulated irregular network (TIN) model and barycentric coordinate system. First row: flat roofs; second row: pent roofs; third row: gable roofs; and fourth row: hip roofs. First column: three-storey models (red) vs. two-storey models (black); second column: two-storey models (black) vs. damaged models (green); third column: two-storey models (black) vs. collapsed models (blue). r is the correlation coefficient between the 3D shape signature curves of two models.

2.4 *Results from real LiDAR data for 3D buildings*

Buildings in the real world may be more complex than the four basic models in figure 2, but the new method in §2.3 can still be applied to LiDAR data for real buildings. Since it is difficult to find sample buildings that have pre-earthquake 3D information and post-earthquake LiDAR data, a small LiDAR data set in Harris County, TX, USA was used for 3D shape signature analysis of real buildings. Although the data set was not related to post-earthquake building damage, it can be used to demonstrate the performance of 3D shape signatures in revealing changes in 3D building shapes. In figure 7(*a*), the upper part shows a TIN model built from LiDAR data for six buildings, and the lower part is an air photo of the six buildings. The LiDAR point density

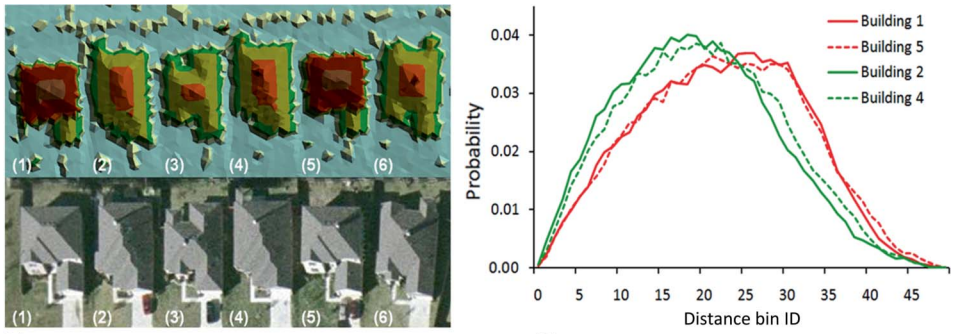

(*a*) (*b*)

Figure 7. 3D shape signature analysis using Light Detection and Ranging (LiDAR) data for selected buildings in Harris County, TX, USA. (*a*) Triangulated irregular network (TIN) model built from LiDAR (top), and air photo (bottom); the numbers in brackets are the building numbers. (*b*) 3D shape signatures derived from LiDAR data of selected buildings.

Table 1. Correlation coefficients between 3D shape signatures of selected buildings.

	Building 1	Building 2	Building 4	Building 5
Building 1	1	0.8702	0.9271	**0.9962**
Building 2	0.8702	1	**0.9902**	0.8726
Building 4	0.9271	**0.9902**	1	0.9308
Building 5	**0.9962**	0.8726	0.9308	1

Note: Bold numbers show high correlation coefficients between the building models of the same type.

is approximately 0.8 point m^{-2}. The 3D shape signatures derived from the LiDAR data for buildings 1, 2, 4 and 5 are shown in figure 7(*b*), and the correlation coefficients between the 3D shape signatures are listed in table 1. The results from 3D shape signature analyses are in accord with those from visual interpretation of the air photo: buildings 1 and 5 are the same model, while buildings 2 and 4 belong to a different model. This example shows that major changes in 3D building shapes can be detected by 3D shape signatures obtained from LiDAR data. Following the same logic, if pre-earthquake 3D shape signatures of a building are known, it is possible to detect severe damage or collapse of the building by comparing its pre-earthquake 3D shape signatures with post-earthquake 3D shape signatures derived from LiDAR data. This also means that only post-earthquake LiDAR data collection is required if pre-earthquake 3D shape signatures are available from other sources such as 3D building models and GIS databases.

3. Sensitivity analyses

In §2.4, results from simple building models with rectangular footprints and real buildings with complex footprints are discussed. These results were based on a random sampling density of approximately 2 points m^{-2}. This brought up two important questions: (1) Do 3D shape signatures of buildings change with LiDAR point density? (2) Are 3D shape signatures of buildings seriously affected by the new data points

generated in TIN triangles? Sensitivity analyses were carried out to answer these questions.

Because of its relatively complex shape compared with the other three building models, the hip roof model (figure 2(*k*)) was selected for the sensitivity test. Simulated LiDAR points were collected from the hip roof with the point density $D = 0.1$, 0.25, 0.5, 1.0, 1.5, 2.0, 2.5, 3.0, 3.5, 4.0, 4.5 and 5.0 points m^{-2}. TIN models were then generated from the simulated LiDAR points and random points inside the building footprint and TIN triangles using the new method described in §2.4. Finally, 3D shape signatures were calculated from the points for the building model using 100 000 random point pairs. Table 2 shows the correlation coefficients between the 3D shape signatures (figure 8(*a*)) when LiDAR point density D changes from 0.1 to 5.0 point m^{-2}. It can be seen that the 3D shape signatures are highly correlated, with correlation coefficients over 0.99 except a few numbers that are slightly less than 0.99 when $D = 0.1$ or 0.25 points m^{-2}. Figure 8(*b*) shows the 3D shape signatures when LiDAR point density is 0.5 point m^{-2} or higher, with corresponding correlation coefficients highlighted in the shaded area of table 2. The results suggest that 3D shape signatures of buildings do not change with LiDAR point density significantly if the LiDAR point density is over a certain level. Because buildings in the real world can be more complex than the hip roof model, it is suggested that a minimum LiDAR point density of 0.5 point m^{-2} is used for 3D shape signature analysis for post-earthquake building damage assessment.

The effects of new data points generated in TIN triangles on the 3D shape signatures of buildings were also studied using the LiDAR data for Building 1 in figure 7. New points were generated in TIN triangles so that point density changed from the original 0.8 point m^{-2} to 1.0, 2.0, 3.0, 4.0 and 5.0 points m^{-2}, respectively. The model was run 3 times at each point density level. The 3D shape signatures are shown in figure 8(*c*), and the correlation coefficients between the 3D shape signatures are listed in table 3. These results show that if the LiDAR point density (0.8 point m^{-2} in this case) is sufficient for 3D shape signature analysis of buildings, the density of the new data points generated in TIN triangles do not change 3D shape signatures of buildings significantly. However, as described in §2.4, these generated data points are necessary for better chararacterization of 3D building shapes.

4. A framework for automated assessment of post-earthquake building damage

Built upon the literature review in §1, the methods in §2 and the results in §3, a framework is proposed for automated assessment of post-earthquake building damage using LiDAR data and GIS. Compared with the tiered reconnaissance system proposed by Adams *et al*. (2004), this framework focuses on per-building (Tier 3) assessment. Assessment at regional (Tier 1) and neighbourhood (Tier 2) levels can be incorporated later to form a broader framework. The current framework has four major components (figure 9): (1) post-earthquake LiDAR data collection and pre-processing; (2) building database and analysis tools in GIS; (3) building damage detection based on 3D shape signatures; and (4) automated GIS database updating.

A flowchart is illustrated in figure 10 to better describe the framework. The input to the flowchart comes from two different sources: (1) post-earthquake LiDAR data and (2) building information from existing GIS databases. In addition to building footprints, the GIS databases should have pre-earthquake 3D shape signatures, or relevant 3D building models and parameters that can be used to calculate 3D shape signatures. For simple buildings with rectangular footprints such as the four models used

Table 2. Correlation coefficients between the 3D shape signatures in figure 8(*a*).

	$D = 0.1$	$D = 0.25$	$D = 0.5$	$D = 1.0$	$D = 1.5$	$D = 2.0$	$D = 2.5$	$D = 3.0$	$D = 3.5$	$D = 4.0$	$D = 4.5$	$D = 5.0$
$D = 0.1$	1	0.9944	0.9846	0.9796	0.9834	0.9810	0.9900	0.9872	0.9892	0.9942	0.9922	0.9894
$D = 0.25$	0.9944	1	0.9897	0.9839	0.9877	0.9891	0.9911	0.9892	0.9920	0.9952	0.9921	0.9910
$D = 0.5$	0.9846	0.9897	1	0.9976	0.9986	0.9966	0.9971	0.9967	0.9957	0.9933	0.9957	0.9943
$D = 1.0$	0.9796	0.9839	0.9976	1	0.9991	0.9959	0.9962	0.9968	0.9961	0.9906	0.9947	0.9921
$D = 1.5$	0.9834	0.9877	0.9985	0.9991	1	0.9965	0.9973	0.9975	0.9961	0.9930	0.9968	0.9940
$D = 2.0$	0.9810	0.9891	0.9966	0.9959	0.9965	1	0.9958	0.9963	0.9968	0.9907	0.9942	0.9948
$D = 2.5$	0.9900	0.9911	0.9971	0.9962	0.9973	0.9958	1	0.9979	0.9982	0.9957	0.9983	0.9974
$D = 3.0$	0.9872	0.9892	0.9967	0.9968	0.9975	0.9963	0.9979	1	0.9980	0.9946	0.9982	0.9968
$D = 3.5$	0.9892	0.9920	0.9957	0.9961	0.9961	0.9968	0.9982	0.9980	1	0.9947	0.9977	0.9981
$D = 4.0$	0.9942	0.9951	0.9933	0.9906	0.9930	0.9907	0.9957	0.9946	0.9947	1	0.9971	0.9941
$D = 4.5$	0.9922	0.9921	0.9957	0.9946	0.9964	0.9942	0.9983	0.9982	0.9977	0.9971	1	0.9972
$D = 5.0$	0.9894	0.9910	0.9943	0.9921	0.9940	0.9948	0.9974	0.9968	0.9981	0.9941	0.9972	1

Notes: *D*, point density. The shaded numbers are the correlation coefficients for the 3D shape signatures in figure 8(*b*).

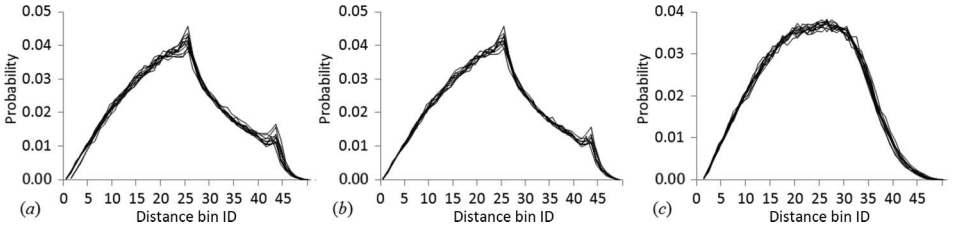

Figure 8. Sensitivity analyses of 3D shape signatures. (*a*) 3D shape signatures of the hip roof model when Light Detection and Ranging (LiDAR) point density changes from 0.1 to 5.0 point m^{-2}; (*b*) 3D shape signatures of the hip roof model when LiDAR point density changes from 0.5 to 5.0 point m^{-2}; and (*c*) 3D shape signatures of Building 1 in figure 7 when the point density changes from 1 to 5.0 points m^{-2}.

Table 3. Correlation coefficients between the 3D shape signatures in figure 8(*c*).

	$D = 1.0$	$D = 2.0$	$D = 3.0$	$D = 4.0$	$D = 5.0$
$D = 1.0$	1	0.9957	0.9987	0.9982	0.9971
$D = 2.0$	0.9957	1	0.9945	0.9980	0.9935
$D = 3.0$	0.9987	0.9945	1	0.9981	0.9972
$D = 4.0$	0.9982	0.9980	0.9981	1	0.9927
$D = 5.0$	0.9971	0.9935	0.9972	0.9927	1

Note: D, point density

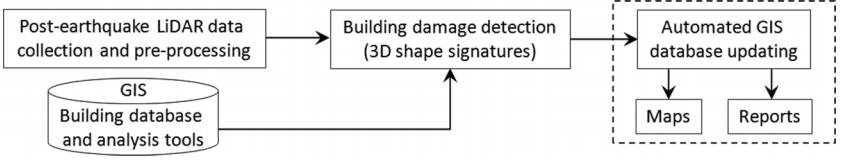

Figure 9. A framework for automated assessment of post-earthquake building damage using Light Detection and Ranging (LiDAR) data and Geographic Information System (GIS).

in §2.2, a 3D model for the building can be built on-the-fly in computer memory once the building parameters such as maximum roof height, minimum roof height, roof type (flat, pent, gable and hip) and ridge length (for hip roofs) are retrieved from the GIS database, thereby 3D shape signatures of the building can be obtained in less than 1 s (see test results on processing time in §2.3). For complex buildings such as those in figure 7, 3D shape signatures or 3D models developed from AutoCAD drawings, aerial images, previous LiDAR and other sources can be stored in GIS. The 3D shape signatures of each complex building can also be calculated in less than 1 s. The pre-earthquake 3D shape signatures are compared with post-earthquake 3D shape signatures derived from LiDAR data using correlation coefficients, and a threshold R_T is used to detect severely damaged (or collapsed) buildings. From the models and samples described in §3, it seems that R_T can be set to 0.99, but users can adjust this threshold based on field observations. As can be seen in figure 10, the process of detecting damaged/collapsed buildings is designed as an automated loop structure, until all buildings are processed. The damaged/collapsed building IDs can be automatically updated in the GIS database for rapid generation of maps and reports.

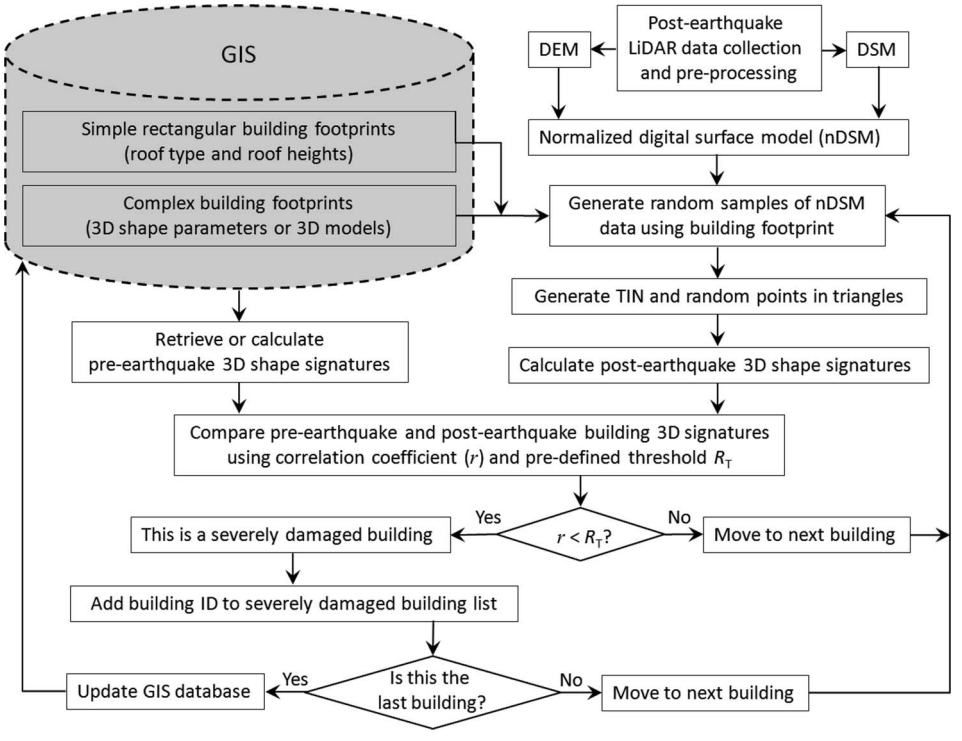

Figure 10. Flowchart for automated assessment of post-earthquake building damage.
Note: GIS, Geographic Information System; TIN, triangulated irregular network; DEM, digital elevation model; DSM, digital surface model.

5. Discussions and conclusion

Five major advantages and two limitations of the proposed frameowrk are discussed below:

1. The framework would work in a more straightforward way if both pre-earthquake and post-earthquake LiDAR data sets are available. If pre-earthquake LiDAR data are not available, the framework will need 3D building information from GIS databases. In rural and sub-urban areas of developing countries, many buildings have relatively simple shapes – usually the four models used in this study. This means updating pre-earthquake building databases with basic building parameters (roof type, maximum roof height and minimum roof height) through field work might be more cost-effective than building 3D models from pre-earthquake high-resolution images and/or LiDAR data. In such cases, efforts of building 3D models can be focused on buildings with more complex 3D shapes. With the emergence of digital earth concepts and infrastructure, it is expected that more and more 3D buidling information can be used to support the framework.
2. The use of LiDAR data in the framework eliminated many limitations of previous methods for building damage assessment using optical or SAR images. For example, the loss of the first floors of buildings is a common damage type in strong earthquakes, and there is no effective way for rapid detection of this

type of damage using optical or SAR images. As demonstrated in this article, the loss of the first floors of buildings can be effectively detected using 3D shape signatures derived from LiDAR data and GIS. With the support of GIS, each individual building is automatically assessed following the building footprints, which also excludes background clutter effects.

3. Since the calculation of 3D shape signatures involves a large number of random point pairs (100 000 pairs in this study) for each building, the results are less sensitive to noise and small changes in 3D shapes. For example, Building 1 in figure 7 has an extra fence segment on the left side of the front yard whereas Building 5 does not have such a feature. Even though the fence segment is visible in LiDAR data, it does not have major influence on the 3D shape signatures, and the two buildings that were made from the same model still have very close 3D shape signatures. The relatively insensitive property of 3D shape signatures also suggests that minor modifications in 3D building shapes (such as the presence or absence of chimneys and solar panels) do not change the 3D shape signatures of the buildings significantly.
4. Similar to (3) above, 3D shape signatures should be relatively tolerant to inaccuracies of building parameters in GIS databases. For example, the 3D shape signatures of a flat building with actual roof height of 3.8 m might not change significantly if the height was estimated and input in the GIS database as 4 m. However, the relationships between geospatial database accuracy (including misalignment between pre- and post-earthquake LiDAR data if pre-earthquake LiDAR data are available) and 3D shape signatures of buildings could be a separate topic for further research.
5. The proposed framework can be made fully automated once the input data are available. The processing speed of approximately one building per second is very promising for building damage assessment following disasters in large geographic areas. With improvements in computing power and algorithm optimization, it is possible that the processing speed can be improved. In addition, it is possible to reduce the number of random point pairs from 100 000 to 50 000 to further improve the procesing speed while keeping the effectiveness of the methods.
6. Because of the reason discussed in (3), one limitation of 3D shape signatures derived from LiDAR and GIS data for building damage assessment is that minor damages to buildings may not be detected. However, this limitation should not be a major problem because a top priority after earthquakes is to detect severely damaged or collapsed buildings and to save people's lives in a timely manner.
7. Finally, for areas with heavy tree canopy coverage, building footprints in GIS databases may not match features in LiDAR data because a building may be partly or totally covered with tree branches. Effective extraction of roof surfaces covered with tree branches remains a future research topic.

In this article, a new method was proposed for more accurate characterization of 3D shape signatures of buildings. The new method involves normalized digital surface models derived from LiDAR data, TIN generation and random points in TIN triangles generated with barycentric coordinates. The new method was applied to four simulated basic building models to test the detection of changes in 3D building shapes in a post-earthquake scenario: (1) a three-storey building model becomes

two-storey after losing the first floor; (2) severe damage of a two-storey building model; and (3) total collapse of a two-storey building model. The new method was then applied to real LiDAR data from four buildings in Harris County, TX, USA. All the changes in 3D shapes of the models and real buildings were successfully detected using 3D shape signatures. Sensitivity analyses were carried out to test the possible influence of LiDAR point density and new points in TIN triangles on 3D shape signatures. The results suggest that LiDAR point density of 0.5 point m^{-2} or higher can generate stable 3D shape signatures of buildings, and that the density of the new points in TIN triangles does not affect 3D shape signatures significantly.

Based on these results, a framework was proposed for automated assessment of post-earthquake building damage using geospatial data. A flowchart was presented to provide more details of the framework. The advantages of the framework include its insensitivity to noise and small variations in 3D building shapes, tolerance to inaccuracies in GIS databases, cost-effectiveness in rural and sub-urban areas of developing countries, fully automated process and computational efficiency. Although the framework cannot detect minor damages to buildings, this limitation should not be a major issue because a top priority in a post-earthquake scenario is to detect severely damaged or collapsed buildings in a timely manner. Due to the lack of real world data sets with both 3D building information in GIS databases and post-earthquake LiDAR data, large-scale case studies were not provided in this article, and further research is needed in this direction. Nonetheless, enough details of the solutions and supportive results were provided using simulated buildings models and real LiDAR data for buildings. It is expected that the framework can be effectively applied to post-earthquake building damage assessment and other disasters that involve major changes in 3D building shapes.

Acknowledgements

This research was supported by the National Basic Research Programme of China (No. 2009CB723906) and a Faculty Research Grant (GA9160) from the University of North Texas, Denton, TX, USA. The authors thank the Chester Carlson Center for Imaging Sciences at the Rochester Institute of Technology (RIT), Rochester, NY, USA, for providing the Haiti earthquake LiDAR data and damage locations.

References

Adams, B.J., 2004, Improved disaster management through post-earthquake building damage assessment using multitemporal satellite imagery. In *Proceedings of the ISPRS XXth Congress*, Vol. XXXV, 12–23 July 2004, Istanbul, Turkey.

Adams, B.J., Ghosh, S., Wabnitz, C. and Alder, J., 2005, Post-tsunami urban damage assessment in Thailand, using optical satellite imagery and theVIEWSTM field reconnaissance system. In *Proceedings of the Conference on the 250th Anniversary of the 1755 Lisbon Earthquake*, 1–4 November 2005, Lisbon, Portugal.

Adams, B.J., Huyck, C.K., Mansouri, B., Eguchi, R.T. and Shinozuka, M., 2004, Application of high-resolution optical satellite imagery for post-earthquake damage assessment: the 2003 Boumerdes (Algeria) and Bam (Iran) earthquakes. In *MCEER Research and Accomplishments 2003–2004*, pp. 173–186 (Buffalo, NY: MCEER).

Adams, B.J., Mansouri, B. and Huyck, C.K., 2006, Streamlining Post-earthquake data collection and damage assessment in Bam, using VIEWS (Visualizing Impacts of Earthquake

with Satellites). *Earthquake Spectra Special Issue 1 (December 2005), 2003 Bam, Iran, Earthquake Reconnaissance Report* (Oakland, CA: EERI).

Ahmadi, S., Zoej, M.J., Ebadi, H., Moghaddam, H.A. and Mohammadzadeh, A., 2010, Automatic urban building boundary extraction from high resolution aerial images using an innovative model of active contours. *International Journal of Applied Earth Observation and Geoinformation*, **12**, pp. 150–157.

Alexander, C., Smith-Voysey, S., Jarvis, C. and Tansey, K., 2009, Integrating building footprints and LiDAR elevation data to classify roof structures and visualise buildings. *Computers, Environment and Urban Systems*, **33**, pp. 285–292.

Aoki, H., Matsuoka, M. and Yamazaki, F., 1998, Characteristics of satellite SAR images in the damaged areas due to the Hyogoken-Nanbu earthquake. In *Proceedings of the 1998 Asian Conference on Remote Sensing*, 16–20 November 1998, Manila.

Baltsavias, E.P., 2004, Object extraction and revision by image analysis using existing geodata and knowledge: current status and steps towards operational systems. *ISPRS Journal of Photogrammetry and Remote Sensing*, **58**, pp. 129–151.

Baltsavias, E.P., Mason, S. and Stallmann, D., 1995, Use of DTMs/DSMs and orthoimages to support building extraction. In *Automatic Extraction of Man-Made Objects From Aerial and Space Images*, A. Grün, O. Kübler and P. Agouris (Eds.), pp. 199–210 (Basel: Birkhäuser Verlag).

Barsi, A., 2004, Object detection using neural self-organisation. *The International Archives of the Photogrammetry, Remote Sensing and Spatial Information Sciences*, **XXXV**, pp. 366–371.

Bellman, C.J. and Shortis, M.R., 2004, A classification approach to finding buildings in large scale aerial photographs. *The International Archives of the Photogrammetry, Remote Sensing and Spatial Information Sciences*, **XXXV**, pp. 337–342.

Bradley, C.J., 2007, *The Algebra of Geometry: Cartesian, Areal and Projective Co-Ordinates* (Bath: Highperception).

Brenner, C., 2005, Building reconstruction from images and laser scanning. *International Journal of Applied Earth Observation and Geoinformation*, **6**, pp. 187–198.

Chen, Z. and Hutchinson, T.C., 2010, Probabilistic urban structural damage classification using bitemporal satellite images. *Earthquake Spectra*, **26**, pp. 87–109.

Chiroiu, L., Andre, G., Guillande, R. and Bahoken, F., 2002, Earthquake damage assessment using high resolution satellite imagery. In *Proceedings of the 7th National US Conference on Earthquake Engineering*, 21–25 July 2002, Boston, MA.

Dong, P., 2009, Characterization of individual tree crowns using three-dimensional shape signatures derived from LiDAR data. *International Journal of Remote Sensing*, **30**, pp. 6621–6628.

Dong, P., 2010, Sensitivity of LiDAR-derived three-dimensional shape signatures for individual tree crowns: a simulation study. *Remote Sensing Letters*, **1**, pp. 159–167.

Dong, Y., Li, Q., Dou, A. and Wang, X., 2011, Extracting damages caused by the 2008 Ms 8.0 Wenchuan earthquake from SAR remote sensing data. *Journal of Asian Earth Sciences*, **40**, pp. 907–914.

Elwood, S., 2008, Volunteered geographic information: future research directions motivated by critical, participatory, and feminist GIS. *GeoJournal*, **72**, pp. 173–183.

Flanagin, A.J. and Metzger, M.J., 2008, The credibility of volunteered geographic information. *GeoJournal*, **72**, pp. 137–148.

Goodchild, M.F., 2007, Citizens as sensors: the world of volunteered geography. *GeoJournal*, **69**, pp. 211–221.

Goodchild, M.F., 2009, NeoGeography and the nature of geographic expertise. *Journal of Location Based Services*, **3**, pp. 82–96.

Gould, M., 2006, The high and low roads. *GeoConnexion Magazine*, May, p. 24.

Gruen, A., 1998, TOBAGO - a semi-automated approach for the generation of 3-D building models. *ISPRS Journal of Photogrammetry and Remote Sensing*, **53**, pp. 108–118.

Guo, H., Li, X. and Zhang, L., 2009, Study of detecting method with advanced airborne and spaceborne synthetic aperture radar data for collapsed urban buildings from the Wenchuan earthquake. *Journal of Applied Remote Sensing*, **3**, pp. 2–19.

Haala, N. and Brenner, C., 1999, Extraction of buildings and trees in urban environments. *ISPRS Journal of Photogrammetry and Remote Sensing*, **54**, pp. 130–137.

Huyck, C.K., Mansouri, B., Eguchi, R.T., Houshmand, B., Castner, L.L. and Shinozuka, M., 2002, Earthquake damage detection algorithms using optical and ERS-SAR satellite data – application to the August 17, 1999 Marmara, Turkey earthquake. In *Proceedings of the 7th National US Conference on Earthquake Engineering*, 21–25 July 2002, Boston, MA.

Ioannidis, C., Psaltis, C. and Potsiou, C., 2009, Towards a strategy for control of suburban informal buildings through automatic change detection. *Computers, Environment and Urban Systems*, **33**, pp. 64–74.

Jang, K.H. and Jung, S.K., 2009, Practical modeling technique for large-scale 3D building models from ground images. *Pattern Recognition Letters*, **30**, pp. 861–869.

Kabolizade, M., Ebadi, H. and Ahmadi, S., 2010, An improved snake model for automatic extraction of buildings from urban aerial images and LiDAR data. *Computers, Environment and Urban Systems*, **34**, pp. 435–441.

Kaya, S., Curran, P.J. and Llewellyn, G., 2005, Post-earthquake building collapse: a comparison of government statistics and estimates derived from SPOT HRVIR data. *International Journal of Remote Sensing*, **26**, pp. 2731–2740.

Li, M., Cheng, L., Gong, J., Liu, Y., Chen, Z., Li, F., Chen, G., Chen, D. and Song, X., 2008, Post-earthquake assessment of building damage degree using LiDAR data and imagery. *Science in China Series E: Technological Sciences*, **51**, pp. 133–143.

Maas, H.-G. and Vosselman, G., 1999, Two algorithms for extracting building models from raw laser altimetry data. *ISPRS Journal of Photogrammetry and Remote Sensing*, **54**, pp. 153–163.

Madhavan, B., Wang, C., Tanahashi, H., Hirayu, H., Niwa, Y., Yamamoto, K., Tachibana, K. and Sasagawa, T., 2006, A computer vision based approach for 3D building modelling of airborne laser scanner DSM data. *Computers, Environment and Urban Systems*, **30**, pp. 54–77.

Matsuoka, M. and Yamazaki, F., 2002, Application of the damage detection method using SAR intensity images to recent earthquakes. In *Proceedings of the IGARSS*, 24–28 June 2002, Toronto, ON.

Mayer, H., 2008, Object extraction in photogrammetric computer vision. *ISPRS Journal of Photogrammetry and Remote Sensing*, **63**, pp. 213–222.

Nixon, M. and Aguado, A.S., 2002, *Feature Extraction and Image Processing*, pp. 220–243 (Oxford, UK: Newnes).

Oriot, H., 2003, Statistical snakes for building extraction from stereoscopic aerial images. *The International Archives of the Photogrammetry, Remote Sensing and Spatial Information Sciences*, **XXXIV**, pp. 65–70.

Osada, R., Funkhouser, T., Chazelle, B. and Dobkin, D., 2002, Shape distribution. *ACM Transactions on Graphics*, **21**, pp. 807–832.

Pesaresi, M. and Benediktsson, J.A., 2001, A new approach for the morphological segmentation of high-resolution satellite imagery. *IEEE Transaction on Geosciences and Remote Sensing*, **39**, pp. 309–320.

Pu, S. and Vosselman, G., 2009, Knowledge based reconstruction of building models from terrestrial laser scanning data. *ISPRS Journal of Photogrammetry and Remote Sensing*, **64**, pp. 575–584.

Rottensteiner, F., Trinder, J., Clode, S. and Kubik, K., 2005, Using the Dempster–Shafer method for the fusion of LIDAR data and multi-spectral images for building detection. *Information Fusion*, **6**, pp. 283–300.

Saito, K., Spence, R.J., Going, C. and Markus, M., 2004, Using high-resolution satellite images for post-earthquake building damage assessment: a study following the 26.1.01 Gujarat earthquake. *Earthquake Spectra*, **20**, pp. 145–170.

Sithole, G. and Vosselman, G., 2004, Experimental comparison of filter algorithms for bare earth extraction from airborne laser scanning point clouds. *ISPRS Journal of Photogrammetry and Remote Sensing*, **59**, pp. 85–101.

Stilla, U. and Jurkiewicz, K., 1999, Reconstruction of building models from maps and laser altimeter data. In *Integrated Spatial Databases: Digital Images and GIS*, P. Agouris and A. Stefanidis (Eds.), pp. 34–46 (Berlin: Springer).

Stilla, U., Soergel, U. and Thoennessen, U., 2003, Potential and limits of InSAR data for building reconstruction in built-up areas. *ISPRS Journal of Photogrammetry and Remote Sensing*, **58**, pp. 113–123.

Sugihara, K. and Hayashi, Y., 2008, Automatic generation of 3D building models with multiple roofs. *Tsinghua Science and Technology*, **13**, pp. 368–374.

Suveg, I. and Vosselman, G., 2004, Reconstruction of 3D building models from aerial images and maps. *ISPRS Journal of Photogrammetry and Remote Sensing*, **58**, pp. 202–224.

Tang, P., Huber, D., Akinci, B., Lipman, R. and Lytle, A., 2010, Automatic reconstruction of as-built building information models from laser-scanned point clouds: a review of related techniques. *Automation in Construction*, **19**, pp. 829–843.

Tovari, D. and Pfeifer, N., 2005, Segmentation based robust interpolation – a new approach to laser data filtering. *The International Archives of the Photogrammetry, Remote Sensing and Spatial Information Sciences*, **XXXVI**, pp. 79–84.

Turker, M. and Sumer, E., 2008, Building-based damage detection due to earthquake using the watershed segmentation of the post-event aerial images. *International Journal of Remote Sensing*, **29**, pp. 3073–3089.

Turner, A., 2006, *Introduction to Neogeography*. O'Reilly Short Cuts Series, 54 p. (Sebastopol, CA: O'Reilly Media). Available online at: http://brainoff.com/iac2009/IntroductionToNeogeography.pdf

Vu, T.T., Yamazaki, F. and Matsuoka, M., 2009, Multi-scale solution for building extraction from LiDAR and image data. *International Journal of Applied Earth Observation and Geoinformation*, **11**, pp. 281–289.

Wang, C., Zhang, H., Wu, F., Zhang, B., Tang, X., Wu, H., Wen, X. and Yan, D., 2009, Disaster phenomena of Wenchuan earthquake in high resolution airborne synthetic aperture radar images. *Journal of Applied Remote Sensing*, **3**, pp. 20–35.

Weidner, U. and Förstner, W., 1995, Towards automatic building extraction from high-resolution digital elevation models. *ISPRS Journal of Photogrammetty and Remote Sensing*, **50**, pp. 38–49.

Yusuf, Y., Matsuoka, M. and Yamazaki, F., 2002, Detection of building damage due to the 2001 Gujurat, India Earthquake, using satellite remote sensing. In *Proceedings of the 7th National US Conference on Earthquake Engineering*, 21–25 July 2002, Boston, MA.